Pore size effect of 1,3,6,8-tetrakis(4-carboxyphenyl)pyrene-based metal-organic frameworks for enhanced SF_6 adsorption with high selectivity

Michelle Åhlén [a], Francoise M. Amombo Noa [b], Lars Öhrström [b], Daniel Hedbom [a], Maria Strømme [a], Ocean Cheung [a,*]

[a] *Division of Nanotechnology and Functional Materials, Department of Materials Science and Engineering, Uppsala University, Ångström Laboratory, Uppsala, SE-751 03, Box 35, Sweden*
[b] *Chemistry and Biochemistry, Department of Chemistry and Chemical Engineering, Chalmers University of Technology, Gothenburg, SE-41296, Sweden*

ABSTRACT

Anthropogenic greenhouse gas emission poses as serious threat to our environment and it is therefore of utmost importance that efficient systems are developed to mitigate these issues. SF_6, in particular, has attracted more attention in recent years due to its global warming potential which severely exceeds that of CO_2. In this study we present the SF_6 sorption properties of four highly porous 1,3,6,8-tetrakis(4-carboxyphenyl)pyrene-based ($TBAPy^{4-}$) metal-organic frameworks containing either ytterbium(III), thulium(III), cerium(III), or hafnium (IV). These MOFs can be synthesized with high crystallinity in as little as 5 h and were found to have good SF_6 uptakes due to their suitable pore size. The SF_6 uptake of the Yb-TBAPy MOF reached 2.33 mmol g^{-1} with high Henry's law SF_6-over-N_2 selectivity of ~80 at 1 bar and 293 K. The TBAPy-MOFs were also found to have good chemical stability and good cyclic SF_6 sorption stability with fast SF_6 uptake. These TBAPy-MOFs possesses many of the properties desired for an efficient SF_6 sorbent and may be suitable sorbents for further development, including sorbent processing for industrial applications.

1. Introduction

The effect of increased concentrations of greenhouse gases in the atmosphere has been confidently linked to the observed climate change and global warming in recent years. Of the typical greenhouse gases, carbon dioxide (CO_2) and methane (CH_4) are perhaps the most well-known as they are connected to our everyday lives - e.g. the combustion of fossil fuel, or animal farming. Other greenhouse gases, such as sulfur hexafluoride (SF_6), is less known at least in the mainstream media. SF_6 has excellent dielectric properties, it is non-toxic, and thermally stable. This has made SF_6 a popular choice in a number of applications where these properties are desired, such as in high-voltage systems, circuit breakers, and the semiconductor manufacturing industries. On the other hand, the global warming potential of SF_6 is over 22,000 times higher than that of CO_2 [1], which means that the emission of SF_6 is also a significant contributor to global warming. A number of technological solutions have been employed to reduce the emission of SF_6, these include incineration, SF_6 recirculation, plasma discharge, and radio

frequency discharge etc. However, the removal of SF_6 from its point sources through the use of solid-based adsorption processes has, in recent years, garnered attention and has been proposed as a potentially efficient alternative. Adsorption of SF_6 would require a good adsorbent and a number of potential microporous materials have been considered as candidate sorbents, including zeolites [2,3], porous carbons [4,5], as well as metal-organic frameworks (MOFs) [6,7]. A good adsorbent needs to possess desirable properties, including high capture capacity, good selectivity, low heats of adsorption for easy regeneration, high cycling stability over a number of adsorption cycles and more. Metal-organic frameworks, being a class of porous materials that are constructed from organic linkers coordinating the metal centers, have interesting constructions which allow them to possess enormous structural diversity. Many properties of MOFs can be tailored such as pore size, surface chemistry, flexibility, and stability [6,8]. The diverse structural possibilities and chemistries allow MOFs to be considered as promising functional materials for many applications, which include drug delivery, catalysis, energy conversion, gas sensing, and luminescence-based

sensing [9–14]. Tetratopic pyrene-based organic molecules have shown to be interesting building blocks for the construction of novel MOF structures [15]. Pyrene-based frameworks have successfully been prepared from various main group and transition metals, such as Mg(II) [16–18], Zn(II) [19–22], Ni(II) [23], In(III) [24], Eu(III) [25], Zr(IV) [26], Hf(IV) [27], and U(IV) [28,29], resulting in a large number of MOFs with diverse structural features. Examples of such features can be seen in many 1,3,6,8-tetrakis(4-carboxyphenyl)pyrene-based frameworks such as the 3D indium(II)- and cadmium(II)-based frameworks ROD-7 [24] and ROD-8 [30]. Both ROD-7 and ROD-8 both exhibit structures composed of infinite 1D ROD secondary building units (SBUs) interconnected through the tetratopic pyrene ligands. Forming two types of 1D channels with dimensions of 4.93 × 9.83 Å/6.82 × 8.96 Å along the *b*-axis [24] and 8.5 × 9.5 Å/6.5 × 11.8 Å along the *a*-axis [30] for ROD-7 and ROD-8, respectively. Both frameworks exhibited appreciable porosities – with Brunauer-Emmett-Teller (BET) surface areas ranging from approximately 1189 m^2 g^{-1} for ROD-7 [24] to 369 m^2 g^{-1} for ROD-8 [30]. The CO_2 uptake capacities of the frameworks were not found to correlate to the specific surface areas of the MOFs, as ROD-8 displayed a higher CO_2 adsorption capacity (1.8 mmol g^{-1}) [30] as compared to ROD-7 (1.5 mmol g^{-1}) [31] at 298 K and 1 bar. Although the authors did not provide an explanation for this phenomenon, it may likely be related to the interplanar distance between the pyrene cores in ROD-8 (4.35 Å [30]). The interplanar distance in ROD-8 is closer in distance as compared to ROD-7 (7.12 Å [31]), resulting in an increased interaction between the CO_2 molecules and the pore surface. Similarly, the europium-based ROD-MOF JXNU-5 shares some structural similarities to ROD-7 and ROD-8. The 3D framework possesses 1D channels with apertures of 4.6 Å and 6.7 Å (as determined by nonlocal density functional theory- NLDFT) but has a less symmetric structure due to the inherently different rod-metal-SBU in JXNU-5. The framework was found to have comparable BET surface area (406 m^2 g^{-1}) and CO_2 uptake capacity (1.55 mmol g^{-1} at 298 K and 1 bar) to ROD-7 and ROD-8 despite the slight structural distortion [25]. The formation of framework structures with large pores have also been successfully obtained in the zirconium(IV)- and hafnium(IV)-based pyrene-based frameworks NU-1000 [26,27]. Unlike the previously mentioned ROD-MOFs, Zr- and Hf-NU-1000 exhibit both meso- (31 Å/29 Å) and micropores (12 Å and 8 Å/13 Å) [32] resulting in highly porous frameworks with BET surface areas of 2320/1780 m^2 g^{-1} and a total pore volumes of 1.26/1.14 cm^3 g^{-1} (of which 43% constitutes the micropore volume in Zr-NU-1000) [27,32]. Although the CO_2 uptake capacity of Zr-NU-1000 (7.92 wt%) [31] is comparable to that of ROD-8, it can be assumed that this phenomenon is due to the high porosity and not to an increased CO_2-pore surface interaction, as is evident by the low CO_2 heat of adsorption on Zr-NU-1000 [31]. The pore size of many 1,3,6,8-tetrakis(4-carboxyphenyl)pyrene (TBAPy)-based frameworks has shown to be capable for the sorption of small gaseous adsorbates, such as CO_2 (3.3 Å [33]) and CH_4 (3.8 Å [34]) [19,23,25,31,35], however the relatively large crystallographic pore aperture (>4 Å) of structures such as ROD-7, -8, JXNU-5, and NU-1000 may indicate that pyrene-based frameworks could be promising for the capture of SF_6 (5.5 Å [36]).

In this study, we tested four highly porous MOFs based on TBAPy^{4-} coordinated with different metals, namely ytterbium (Yb(III)), thulium (Tm(III)), cerium (Ce(III)), and hafnium (Hf(IV)). These MOFs are similar to other TBAPy-based MOFs previously reported in literature, including ROD-7 [24], JXNU-5 [25], and Hf-NU-1000 [27]. The sorption properties of these TBAPy-MOFs were examined and specifically the possibility of using these MOFs as SF_6 adsorbents are be discussed.

2. Experimental section

2.1. Materials

Hafnium(IV) chloride (HfCl$_4$), Ytterbium(III) acetate tetrahydrate (Yb(C$_2$H$_3$O$_2$)$_3$·4H$_2$O), and Thulium acetate hydrate (Tm

(C$_2$H$_3$O$_2$)$_3$·xH$_2$O) were purchased from Sigma-Aldrich (USA). Ammonium cerium(IV) nitrate (Ce(NH$_4$)$_2$(NO$_3$)$_6$), *N,N*-dimethylformamide (DMF) were obtained from VWR AB (Sweden) and 1,3,6,8-tetrakis(4-carboxyphenyl)pyrene (H$_4$TBAPy) was purchased from AmBeed Inc. (Arlington, USA).

All solvents and chemicals were used as received without further purification.

2.2. Experimental procedures

2.2.1. Synthesis of Yb-TBAPy

Yb(C$_2$H$_3$O$_2$)$_3$·4H$_2$O (84.45 mg, 0.20 mmol) and H$_4$TBAPy (136.54 mg, 0.20 mmol) were dissolved in 10 ml DMF. The mixture was transferred to a Teflon-lined stainless-steel autoclave and heated in an oven to 200 °C. After 48 h the autoclave was removed from the oven and allowed to cool to ambient temperatures. The product was collected using centrifugation at 3,800 rpm for 10 min, washed in DMF three times, and dried in a ventilated oven at 70 °C.

2.2.2. Synthesis of Tm-TBAPy

The synthesis of Tm-TBAPy was carried out in a similar manner to Yb-TBAPy. Briefly, Tm(C$_2$H$_3$O$_2$)$_3$·xH$_2$O (69.21 mg, 0.20 mmol) and H$_4$TBAPy (136.54 mg, 0.20 mmol) were dissolved in 10 ml DMF. The mixture was heated in a Teflon-lined stainless-steel autoclave and left in an oven at 200 °C. After 48 h the autoclave was removed from the oven and allowed to cool and the product was collected using centrifugation at 3,800 rpm for 10 min, washed with DMF three times, and finally dried in a ventilated oven at 70 °C.

2.2.3. Synthesis of Hf-TBAPy

Hf-TBAPy was synthesized using different procedures than those presented in literature for Hf-NU-1000 [27]. Briefly, a mixture of HfCl$_4$ (128.12 mg, 0.40 mmol) and H$_4$TBAPy (273.08 mg, 0.40 mmol) was dissolved in 10 ml DMF. The mixture was heated in a Teflon-lined stainless-steel autoclave at 200 °C for 24 h, after which the cooled product was collected by centrifugation at 3,8000 rpm for 10min, washed with DMF three times, and dried in a ventilated oven at 70 °C.

2.2.4. Synthesis of Ce-TBAPy

A mixture of Ce(NH$_4$)$_2$(NO$_3$)$_6$ (109.64 mg, 0.20 mmol) and H$_4$TBAPy (136.54 mg, 0.20 mmol) in 10 ml DMF was heated in a Teflon-lined stainless-steel autoclave at 200 °C. The mixture was left in the oven for 5 h and the cooled product was thereafter collected by centrifugation at 3,800 rpm for 10 min, washed with DMF three times, and dried in a ventilated oven at 70 °C.

2.3. Materials characterization

Powder X-ray diffractograms (PXRD) of the synthesized materials were recorded on a Bruker D8 Advance TwinTwin diffractometer (Bremen, Germany) using Cu Kα-radiation (λ = 1.5418 Å) and operated at 40 kV and 40 mA. PXRD data were collected within a 2θ-range of 5–50° using a step-size of 0.015° and a time-per-step of 0.4 s. Scanning electron microscopy (SEM) images were obtained using a Zeiss Merlin Field Emission Scanning Electron Microscope (Oberkochen, Germany) operated at 1 kV and 50 pA. All samples were pre-sputtered using Ag/Pd prior to imaging. Core-level XPS spectra were recorded on a ULVAC-PHI II Scanning XPS Microprobe (Chanhassen, MN, US) using monochromatic Al Kα radiation and Ar$^+$ ions as well as low-energy electrons for charge neutralization. Obtained spectra were calibrated using the C 1s peak for adventitious carbon at 284.8 eV.

2.4. Gas sorption analysis

Equilibrium sorption isotherms were collected on a Micromeritics ASAP2020 surface area analyzer (Norcross, GA, USA) on samples pre-

degassed at 448 K for 3 h under dynamic vacuum (1×10^{-4} Pa) using a Micromeritics SmartVacPrep (Norcross, GA, USA). Langmuir specific surface areas were calculated from nitrogen (N_2) isotherms recorded at liquid nitrogen temperatures (77 K) and the corresponding density functional theory (DFT) pore size distributions were estimated from the N_2 isotherms using the slit pore mode for N_2. CH_4, CO_2, N_2, and SF_6 equilibrium isotherms were recorded using a Micromeritics ASAP2020 surface area analyzer (Norcross, GA, USA) at 273–303 K using an insulated dewar containing temperature adjusted/controlled water or an ice-water slurry. Brunauer-Emmett Teller (BET) was calculated with the recorded isotherm data using the BET surface identification (BETSI) software provided by Adsorption and Advanced Materials Lab (AAML), Department of Chemical Engineering & Biotechnology, University of Cambridge, UK [37]. Gas selectivities for theoretical gas mixtures containing SF_6/N_2 (10:90), CO_2/N_2 (15:85), and CO_2/CH_4 (50:50) were calculated using the Ideal Adsorption Solution Theory (IAST) [38] from single component isotherms recorded at 273–303 K. The CH_4, CO_2, N_2, and SF_6 isotherms were fitted using either the single- or dual-site Langmuir model for the IAST calculations. Henry's law selectivities ($s = K_{H,\ gas\ 1}/K_{H,\ gas\ 2}$) for SF_6/N_2, CO_2/N_2, and CO_2/CH_4 were calculated using the Henry's law constants ($K_{H,\ gas}$) obtained from single component isotherms collected at 273–303 K. Isosteric enthalpies ($-\Delta H_{ads}$) of SF_6, CO_2, and CH_4 adsorption were calculated from isotherms collected at 273–303 K using the Clausius-Clapeyron equation [39]. All isotherms were modeled using either the single- or dual-site Langmuir model.

Gravimetric SF_6 adsorption profiles were obtained using a Mettler Toledo TGA/DSC 3+ (Schwerzenbach, Switzerland) on approximately 15 mg samples at 303 K using a SF_6 flow-rate of 60 ml min^{-1}. All samples were degassed *in-situ* prior to adsorption at 423 K for 1 h in a N_2 atmosphere (60 ml min^{-1}). Further, SF_6 diffusivities were estimated using the intracrystalline diffusion model [40] on corrected gravimetric SF_6 profiles.

2.5. Stability study

The stability of the TBAPy-based MOFs were studied using various aqueous and organic solvents. 5 mg of each sample was stirred in 5 ml of MeOH, EtOH, acetone, toluene, deionized water, 1 M NaOH (aq.), and 1 M HCl (aq.) for 5 h at room temperature. The samples were thereafter collected by centrifugation at 3,800 rpm for 10 min and analyzed using PXRD ($\lambda = 1.5418$ Å). The thermal stability of the samples were investigated using thermogravimetric analysis (Mettler Toledo TGA/DSC 3+, Schwerzenbach, Switzerland). The as-synthesized TBAPy-MOFs were heated from 298 K to 1073 K in the presence of air (60 ml min^{-1} flow-rate).

3. Results and discussion

3.1. Structure of TBAPy-based MOFs

The TBAPy-based MOFs were solvothermally synthesized in DMF at 200 °C yielding yellow and dark orange micro-crystalline products. Despite our best efforts, no single crystals could be grown, but good powder diffractograms were obtained (Fig. 1) showing the products to be crystalline. Thus, while no definite proof of structure can be presented, a discussion based on known chemical similarities of the different metal ions, can be made with similar MOFs and their simulated powder patterns compared with those obtained for the as-synthesized TBAPy-based structures (Fig. 1). The Yb- and Tm-TBAPy MOFs had PXRD patterns that were close to the simulated PXRD pattern of the Eu (III) based JXNU-5 (Fig. S1), which suggested that Yb- and Tm-TBAPy MOFs shared structural similarities to JXNU-5, $(Me_2NH_2)_3[Eu_7(\mu_3-O)_2(TBAPy)_5(H_2O)_6] \cdot 12$ DMF [25]. Pawley refinements account for all except one or two very minor signals (Fig. S1, Table S1) with a weighted profile R-factor, R_{wp}, of 9.9 and 6.2 for Yb- and Tm-TBAPy, respectively. Pawley refinement of the PXRD pattern of Hf-TBAPy fitted well with the
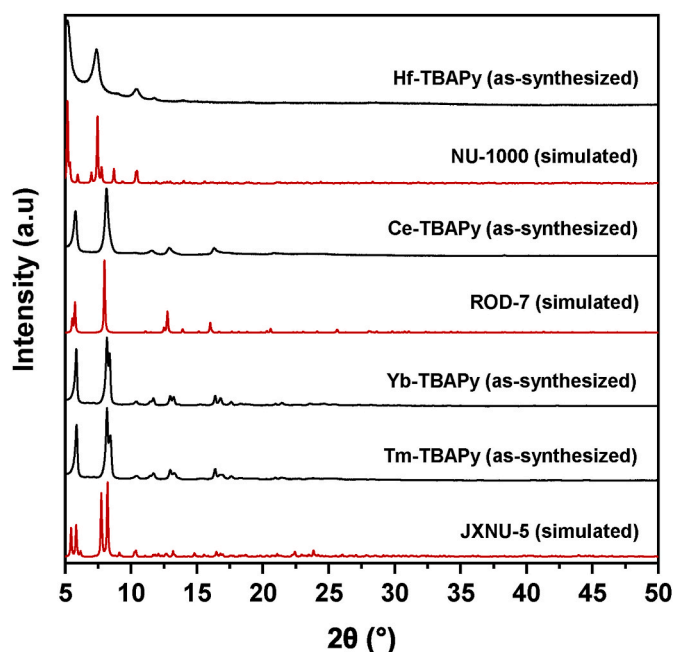

Fig. 1. Powder X-ray diffractograms of the as-synthesized MOFs and the simulated diffraction patterns of ROD-7 [24], JXNU-5 [25], and NU-1000 [26] ($\lambda = 1.5418$ Å).

Zr(IV) MOF Zr-NU-1000, $[Zr_6(\mu_3-OH)_8(OH)_8(TBAPy)_2]$ [26] (Fig. S1, Table S1) with no unexplained features giving a R_{wp}, of 2.7. Significant peak broadening was also noted in this PXRD pattern which was found to be due to the small particle size of this sample (Fig. S3). Ce-TBAPy, on the other hand, appeared closer to ROD-7 and a subsequent Pawley fit gave a R_{wp}, of 7.8, with all peaks except for a small peak at 10.4° and a shoulder at 13.6° accounted for (Fig. S1, Table S1). These two peaks may possibly be related to a small impurity of a JXNU-5-like phase. Based on our data analysis, we suggest that Ce -TBAPy is isoreticular to ROD-7, $[In_2(OH)_2(TBAPy)]$ [24], and Yb- and Tm-TBAPy to JXNU-5. Although ROD-7 and JXNU-5 are rod-MOFs with similar architectures, they however feature different SBUs and thus contain slightly different types of pore channels (Fig. S2). The main difference between JXNU-5 and ROD-7 is that the latter structure possesses straight channels as well as a less complex and more symmetric structure due to a different rod-metal-SBU (Fig. S2). According to the chemical formulas of JXNU-5 [25], ROD-7 [24], and NU-1000 [26] MOFs in literature, the Yb- and Tm-TBAPy were therefore presumed to be $[M_7(\mu3-O)_2(TBAPy)_5(H_2O)_6] \cdot xDMF$ (where M = Yb(III), Tm(III), TBAPy = $C_{44}H_{26}O_8$), Ce-TBAPy to be $[Ce_2(OH)_2(TBAPy)]$, and Hf-TBAPy as $[Hf_6(\mu_3-OH)_8(OH)_8 (TBAPy)_2]$.

SEM images of the TBAPy-based MOFs (Fig. S3) show that the particle size for all samples were in the nanometer (nm) scale. In particular, the particle shape of Yb- and Tm-TBAPy were found to be similar to each other and appeared as small plate-like particles. Ce-TBAPy had a comparatively more distinct shape, the individual particles were also of nm scale in size but appeared to adopt a cross-shape. Microscopically the Ce-TBAPy cross-shape particles assembled to form rounded cube-like aggregated microparticles (Figs. S3c–d). The Hf-TBAPy particles were the smallest of all the TBAPy-MOFs in this study, these somewhat irregularly shaped particles also appear aggregated according to the SEM images (Figs. S3g–h). Increasing the synthesis time of Hf-TBAPy did not noticeably increase the particle size, but yielded samples with decreased porosity. Although Hf-TBAPy is similar to Hf-NU-1000 presented by Beyzavi et al. [27], the particle size and shape of the two materials were noticeably different.

The TGA decomposition profiles of the Yb-, Tm-, and Hf-TBAPy (Fig. S9) revealed that the metal content of these MOFs were reasonably close to the expected values according to their respective chemical

formula (Table S2). Ce-TBAPy contained a lower metal content than expected (when calculated using the assumed chemical formula based on ROD-7) and was found to be related to the presence of residual linker that was not removed despite repeated washing. According to the TG analysis, the residual linker amount was close to 30 wt% (see Fig. S9 and Table S2) which may require supercritical CO_2 washing to remove. Due to the significant presence of residual linker on Ce-TBAPy, we will not focus the discussion on Ce-TBAPy in the rest of this study. Further analyses, including X-ray photoelectron spectroscopy (XPS) (Fig. S10) and gas sorption data (Fig. S21) related to Ce-TBAPy can be found in the Supporting Information for references.

3.2. Pure gas sorption on TBAPy-MOFs

The porosity of the TBAPy-based samples was studied using nitrogen sorption at 77 K (Fig. 2 and Figs. S11–S12). All samples showed IUPAC type I isotherms which are typical of microporous materials [41]. The BET specific surface areas (SSA_{BET}) were found to range between approximately 716–940 m^2 g^{-1} ($SSA_{Langmuir}$ ~750–1000 m^2 g^{-1}) (Figs. S13–S20, Table 1, and Table S3). The hysteresis observed for Hf-TBAPy between p/p_o ~0.43–0.98 may indicate mesoporosity, which has also been observed on NU-1000 [26]. The distinct isotherm shape and the narrow pore size distribution of the 2–3 nm pores of Zr-NU-1000 was not observed for Hf-TBAPy. Furthermore, the SSA_{BET} of Hf-TBAPy in this study was noticeably less than that shown by Beyzavi et al. [27] and may be related to the differences in sample washing procedures, as well as differences in particle size and crystallinity. As a comparison, large single crystals were noted by Beyzavi et al. [27], in contrast to the sub-μm-sized particles observed in this study. Yb-TBAPy was found to have the highest porosity as indicated by the calculated SSAs and pore volume (i.e. 0.35 cm^3 g^{-1}). The recorded SSA_{BET} values of both Yb- and Tm-TBAPy were higher than those presented for Eu-JXNU-5 (406 m^2 g^{-1}). The porosities of the synthesized samples were not found to directly correspond to the atomic mass of the metal cations in the structures, as is evident by the discrepancy in SSA_{BET} between Yb-TBPAy and Tm-TBAPy. This discrepancy between Yb- and Tm-TBAPy (and also with Eu-JXNU-5) was probably related to a difference in crystallinity between the samples.

The calculated density-functional theory pore size distributions (DFT-PSD) of the samples (Fig. S11) showed that Yb- and Tm-TBAPy have the same average pore size distributions, with the most

predominant type of pore bearing a diameter of ~0.64–0.69 nm. A small number of pores with a diameter of approximately 0.72 nm was also observed on these samples. The pore size distributions of Hf-TBAPy differed slightly when compared with Yb- and Tm-TBAPy - only the pores with a diameter of approximately 0.72 nm were observed. In all cases, pores larger than 1 nm were detected, but the differential pore volume of these larger 1 nm pores was noticeably higher on Hf-TBAPy than in the other samples. DFT pore size analyses echoed the observation that Yb- and Tm-TBAPy may indeed have the same structure (i.e. being isoreticular to JXNU-5), which is somewhat different from that of Hf-TBAPy that likely shares structural similarities with NU-1000. It is important to note that the experimentally obtained DFT-PSDs do not represent the true crystallographic pore size of the structures and that the PSDs presented should be taken as estimates and not absolute values. Furthermore, no correlations between the average pore size and the cation radii of the Yb(III) and Tm(III) metal were noted for the two TBAPy-MOFs.

The crystallographic micropore sizes of JXNU-5 and NU-1000 range between 5 and 9 Å [24,42] and may be suitable for SF_6 sorption. We previously demonstrated that pore sizes of ~7 Å could enhance the sorption of SF_6 (5.5 Å kinetic diameter [36]) on mixed-linker ZIF-7-8s [43]. As the TBAPy-MOFs also have pore sizes within the discussed range, the SF_6, as well as CH_4, CO_2, and N_2, sorption equilibrium isotherms were recorded at 273–303 K (Fig. 3, Figs. S21 and S26, Fig. S28, and Fig. S30) in order to study their gas sorption properties. The highest SF_6 uptake at 293 K and 1 bar (Fig. 3 and Table 2) was observed for Yb-TBAPy (2.33 mmol g^{-1}), then Tm-TBAPy (1.83 mmol g^{-1}), and Hf-TBAPy (1.38 mmol g^{-1}). The difference in SF_6 uptake between Yb- and Tm-TBAPy correlated very well and with the recorded SSA_{BET} of the two MOFs (2.78 μmol m^{-2} for Yb-TBAPy and 2.77 μmol m^{-2} for Tm-TBAPy, Table S6), suggesting that the chemistries related to the sorption and uptake capacity of SF_6 (as well as for other gases, as discussed later) of the two MOFs were comparable.

The SF_6 isotherms for the TBAPy-based MOFs also showed a Langmuir shape. Yb- and Tm-TBAPy-MOFs in this study demonstrated that the comparatively smaller pores on these MOFs (~6.4–6.9 Å) could further enhance the sorption of SF_6 when compared with the ~7 Å pores on mixed-linker ZIF-7-8s [43]. Fig. 4 compares the sorption isotherms of the most SF_6 selective ZIF-7-8 in our previous study with Yb-TBAPy, it is clear that the SF_6 sorption isotherm of Yb-TBAPy had a steeper increase in uptake capacity at low pressure when compared with the mixed-linker ZIF-7-8 (Fig. 4a). The same observation was noted for Tm-TBAPy (Fig. 3b). The steep isotherm at low pressure demonstrated the effect of pore size enhanced sorption of SF_6, which is also reflected in the Henry's law SF_6/N_2 selectivity for Yb- and Tm-TBAPy of ~80 (at 293 K) - the highest value of the selected materials (Fig. 4b and Table S9). Note that the sorption of SF_6 on TBAPy-MOFs were exclusively physisorption and was fully reversible (demonstrated by the lack of hysteresis on the desorption isotherm), therefore, no strong interaction between SF_6 and the pore surface was expected (i.e. strong electrostatic interactions or chemisorption). The SF_6 uptake capacity, as discussed early, was entirely dependent on the available BET surface area of the TBAPy-MOF (i.e. no observable effect from the different metals present in the MOF). In the case of Hf-TBAPy it may be assumed that the dimensions of the pores on Hf-TBAPy were less ideal than Yb- and Tm-TBAPy for enhanced interaction with SF_6. In fact, the ~7.2 Å pores on Hf-TBAPy were very similar in size to one type of pores on the mixed-linker ZIF-7-8 (~7.3 Å) [43], and Fig. 4a also shows that the shapes of the SF_6 on these two materials were very comparable. The SF_6 uptake capacity of the TBAPy-based MOFs were found to be similar to other porous sorbents (Table S5) such as DUT-9 (2.32 mmol g^{-1} at 298 K and 1 bar) [44], MIL-101(Cr) (2.01 mmol g^{-1} at 298 K and 1 bar) [44], UiO-66-Zr (1.45 mmol g^{-1} at 293 K and 1 bar) [45], Zeolite-13X (1.75 mmol g^{-1} at 298 K and 1 bar) [45], and CAU-17 (1.45 mmol g^{-1} at 293 K and 1 bar) [46]. However, SF_6 uptake capacity was observed to be lower in other MOFs such as $Zn_4O(dmcpz)_3$ (2.54 mmol g^{-1} at 298 K and 1 bar)
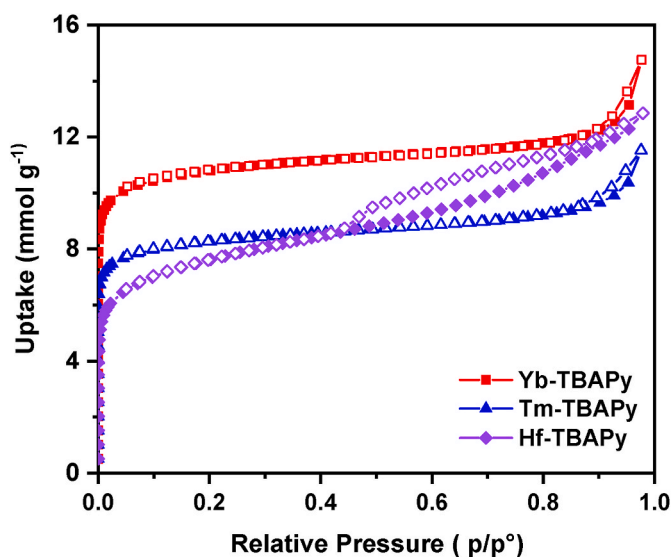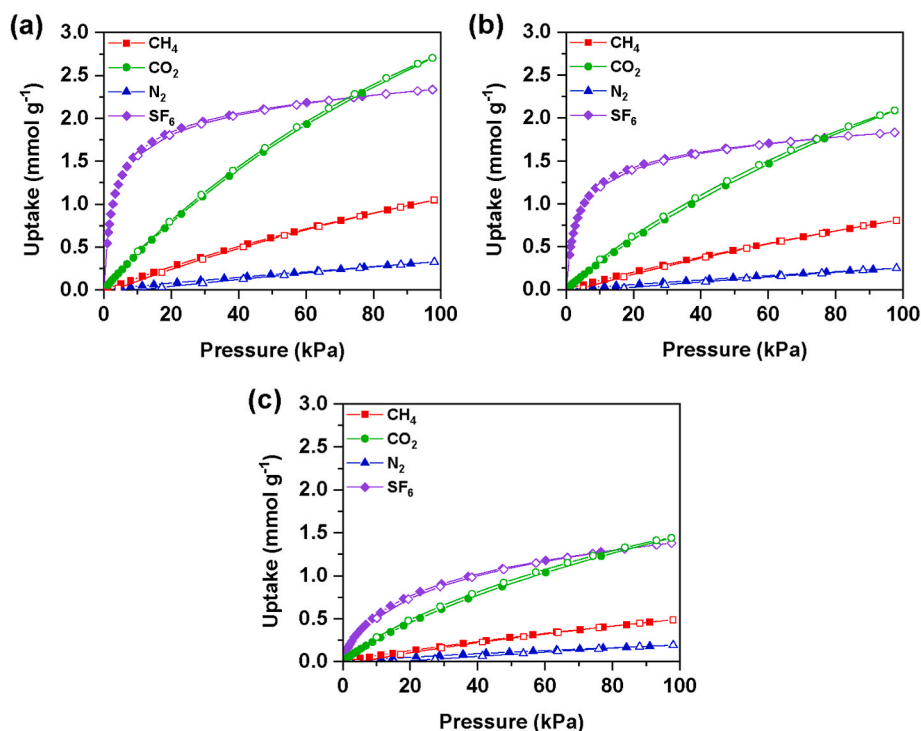

Fig. 2. Equilibrium nitrogen (N_2) sorption isotherms recorded at 77 K. Filled and open symbols represent the adsorption and desorption branches, respectively.

Table 1

Summary of surface area and pore volumes calculated from N_2 sorption isotherms recorded at 77 K for the MOFs.

Sample	$SSA_{Langmuir}$[a] ($m^2 g^{-1}$)	SSA_{BET}[b] ($m^2 g^{-1}$)	V[c] ($cm^3 g^{-1}$)	V_{micro}[d] ($cm^3 g^{-1}$)	V_{meso}[d] ($cm^3 g^{-1}$)
Yb-TBAPy	1065	940	0.35	0.35	–
Tm-TBAPy	815	716	0.33	0.27	–
Hf-TBAPy	760	620	0.45	0.19	0.22

[a] Langmuir specific surface areas ($SSA_{Langmuir}$) were calculated using the Langmuir equation within the pressure range of 4–17 kPa.

[b] Brunauer-Emmett Teller specific surface areas (SSA_{BET}) were calculated using the BETSI software, analysis plots are available in the Supporting Information Fig. S13 – S20.

[c] The representative total pore volumes (V) were calculated using a single point of the adsorption branch at p/p_o 0.90, this pressure point was chosen to avoid the effect of N_2 condensation observed on some samples and a slight underestimation is expected. For Hf-TBAPy the value at p/p_o = 0.98 was used.

[d] The micropore and mesopore volumes (V_{micro}) were estimated using the *t-plot* method.

Fig. 3. CH_4, CO_2, N_2, and SF_6 equilibrium sorption isotherms recorded at 293 K for (a) Yb-TBAPy, (b) Tm-TBAPy, and (c) Hf-TBAPy. Filled and open symbols represent the adsorption and desorption branches, respectively.

Table 2

Summary of CH_4, CO_2, N_2, and SF_6 uptakes at 293 K and 1 bar.

Sample	CH_4 (mmol g^{-1})	CO_2 (mmol g^{-1})	N_2 (mmol g^{-1})	SF_6 (mmol g^{-1})
Yb-TBAPy	1.05	2.70	0.33	2.33
Tm-TBAPy	0.81	2.09	0.25	1.83
Hf-TBAPy	0.49	1.44	0.21	1.38

[44], MIL-100(Fe) (2.60 mmol g^{-1} at 293 K and 1 bar) [45], Zn-MOF-74 (3.80 mmol g^{-1} at 298 K and 1 bar) [47], $Cu_3(btc)_2$ (4.77 mmol g^{-1} at 298 K and 1 bar) [44], Co-MOF-74 (5.30 mmol g^{-1} at 298 K and 1 bar) [47], and Mg-MOF-74 (6.45 mmol g^{-1} at 298 K and 1 bar) [47].

The CO_2 uptake capacity at 1 bar and 293 K was found to be slightly higher as compared to the SF_6 uptakes but was found to follow the same trend. The highest CO_2 uptake was observed in Yb-TBAPy (2.70 mmol g^{-1}, 4.29 μmol m^{-2}) followed by Tm- (2.09 mmol g^{-1}, 4.26 μmol m^{-2}), and Hf-TBAPy (1.44 mmol g^{-1}, 3.45 μmol m^{-2}). A lower affinity between the CO_2 molecules and the pore surface when compared to SF_6 can be assumed due to the isotherm shape, which appeared to be more linear than the SF_6 isotherms. This was somewhat expected as the kinetic

diameter of CO_2 (3.3 Å [33]) is smaller than that of SF_6. The CO_2 uptake in the TBAPy-based samples was found to be comparable to other MOFs such as BUT-11 (2.39 mmol g^{-1} at 298 K and 1 bar) [50], SIFSIX-3-Zn (2.55 mmol g^{-1} at 298 K and 1 bar) [51], SNU-M10 (2.10 mmol g^{-1} at 298 K and 1 bar) [52], and NH_2-MIL-125 (2.18 mmol g^{-1} at 298 K and 1 bar) [53].

The CH_4 uptake was found to be moderately low on all samples (ranging from 0.49 to 1.05 mmol g^{-1} at 293 K and 1 bar) and the shape of the isotherm showed no affinity between the CH_4 molecules and the pore surface of the MOFs. As such, it will not be the focus of the rest of this study, however, data concerning CH_4 sorption on TBAPy-MOFs are documented in the Supporting Information.

3.3. TBAPy-MOFs as selective SF_6 sorbent

In order to consider TBAPy-MOFs as possible SF_6 sorbents, a number of different aspects of the sorption performance need to be evaluated, including the chemical/thermal stability of the sorbent, gas uptake at relevant pressures, selectivity, and sorption kinetics. The chemical and thermal stability of the TBAPy-MOFs in a range of organic solvents as well as at pH 1 and 14 was monitored using PXRD and is discussed in the Supporting Information (Section S3). In short, the synthesized TBAPy-
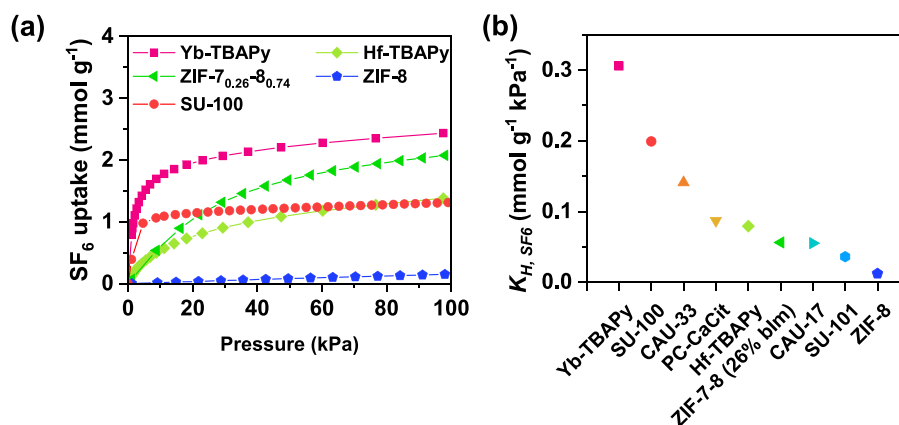
(a)

(b)

Fig. 4. (a) SF_6 sorption isotherms for Yb- and Hf-TBAPy and selected reference materials (SU-100 [48], SU-101 [46], porous carbon (PC-CaCit) [49], ZIF-8 [43], ZIF-$7_{0.26}$-$8_{0.74}$ [43], CAU-33 [46], and CAU-17 [46]) at 293 K and 1 bar (isotherms for SU-100 and PC-CaCit was recorded at 298 K), and b) calculated Henry's law constant ($K_{H,SF6}$) for SF_6 adsorption on Yb-, Hf-TBAPy and selected materials [43,48].

MOFs were found to be stable under the different test conditions, aside from in acidic (1 M HCl, pH 1) and basic (1 M NaOH, pH 14) conditions. The partial pressure of SF_6 in many gas mixtures used in high-voltage circuit breakers is usually kept at ~10 kPa and ~90 kPa N_2 (or other gases). It is therefore of crucial importance to consider the SF_6 uptake capacities of a sorbent at the relevant pressure range in order to evaluate its accessible SF_6 capacity in realistic conditions. The SF_6 adsorption capacity of the TBAPy-based MOFs at 10 kPa was found to be appreciably high and ranged from 0.54 to 1.60 mmol g^{-1} at 293 K. Fig. 5 compares the uptake of SF_6 on different sorbents at 10 kPa (298 K). The low-pressure uptake of SF_6 for the TBAPy-based MOFs was found to be comparable or higher than other sorbents with appreciable SF_6 sorption capacities at 100 kPa, such as DUT-9 (~0.45 mmol g^{-1} at 0.1 bar and 298 K) [44], MIL-100(Fe) (~0.30 mmol g^{-1} at 0.1 bar and 293 K) [45], Zn-MOF-74 (~1.35 mmol g^{-1} at 0.1 bar and 298 K) [47], and $Cu_3(btc)_2$ (~1.12 mmol g^{-1} at 0.1 bar and 298 K) [44] (Fig. 5 and Table S5).

The SF_6/N_2 selectivity of the TBAPy-MOFs were estimated using the Ideal adsorbed solution theory (IAST) as well as the Henry's constants of each gas. IAST selectivities were calculated based on hypothetical gas mixtures containing 10 kPa of SF_6 and 90 kPa N_2. The IAST selectivities

at different temperatures can be found in Fig. 6a, Figs. S22–S25 and are also listed in Table S10. The IAST selectivities of Yb- and Tm-TBAPy were effectively the same across all temperatures, at 293 K the values were 47 and 48 (at 100 kPa). These selectivities are comparable to a number of well-known sorbents, including zeolite 13X (~43 at 293 K and 1 bar) [45] and Zn-MOF-74 (46 at 298 K and 1 bar) [47]. The IAST selectivities of Hf-TBAPy were lower than the other TBAPy-MOFs across all temperatures, this was related to the shape of the SF_6 sorption isotherms, which itself is an effect of the effective pore size as discussed earlier. Interestingly, the IAST selectivities of all Yb- and Tm-TBAPy MOFs increased with increasing temperature, but Hf-TBAPy showed the opposite trend. Henry's law selectivities were also calculated (Table S9) to complement the IAST selectivities, although the Henry's law selectivities were generally higher across all samples than the IAST selectivities, the same increasing/decreasing trend with a change in temperature was also observed. CO_2/N_2 and CH_4/N_2 selectivities (both IAST and Henry's law) were also calculated and presented in the Supporting Information (Tables S10 and S9). These selectivities were not higher than other similar sorbents reported in literature.

The isosteric enthalpies of SF_6 adsorption (-$\Delta H_{ads,SF6}$) was found to range from ~25 to 35 kJ mol^{-1} between 0.3 and 1.1 mmol g^{-1} SF_6 loading (Fig. 6b and Fig. S32). The calculated -$\Delta H_{ads,SF6}$ was found to be within the range typically observed for physisorption, confirming that the adsorbate-adsorbent interaction occurs through weak *VdW* forces [54]. This is to be expected due to the non-polar nature of the SF_6 molecule and confirmed by the lack of hysteresis in the adsorption/desorption isotherms shown in Fig. 3. The -$\Delta H_{ads,SF6}$ can also be seen to decrease slightly with increasing loading for Hf-TBAPy indicating the possibility of preferred adsorption sites. The cyclic SF_6 uptake on the MOFs were also investigated gravimetrically at 303 K (Fig. S33). The SF_6 uptake capacity was found to remain stable for up to 10 cycles and a less than 1 wt% decrease from the first to the last cycle was observed when using mild heating (423 K) to generate the sorbents between each cycle.

The SF_6 adsorption kinetics was investigated gravimetrically at 303 K (Fig. 7). The adsorption rate was found to occur relatively rapidly in the samples, with 80% total uptake being reached after 45–174 s. The SF_6 adsorption kinetics was further investigated gravimetrically at 303 K using approximately 15 mg of sample. The intracrysalline diffusion model was used to evaluate the SF_6 diffusion in the TBAPy-MOFs at both the initial stages of adsorption (Fig. S34a) and at near equilibrium (Fig. S34b). Deviations from the model was observed at both stages of adsorption which may in part be due to heat-transfer effects and external-mass transfer resistance, as a single sample size was used for the analysis and the particle size of the TBAPy-MOFs were found to be within the nm range. The calculated SF_6 diffusivities (Table 3 and Table S16) ranged from ~3×10^{-4} s^{-1} to 6×10^{-4} s^{-1} and were within
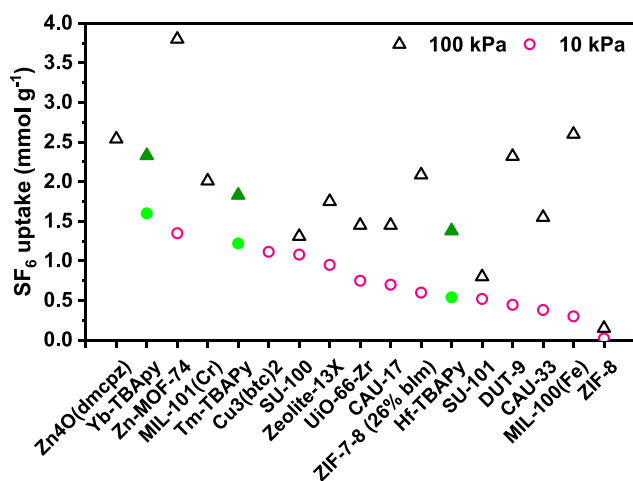

Fig. 5. Comparison of SF_6 uptake capacity of the TBAPy-based MOFs and other porous sorbents at 10 kPa and 100 kPa SF_6. Data for Yb-, Tm-, and Hf-TBAPy are from this study (with green symbols), other data are obtained from literature [43–48] and a tabulated comparison is available in Supporting Information, Table S5. (For interpretation of the references to colour in this figure legend, the reader is referred to the Web version of this article.)
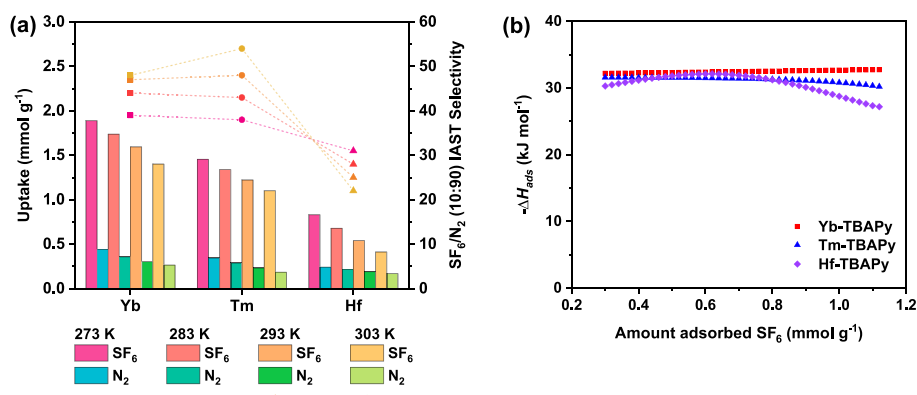
Fig. 6. (a) Low-pressure uptakes of SF_6 (10 kPa) and N_2 (90 kPa) (bars) and the corresponding IAST selectivity (10:90 SF_6/N_2 gas mixture) at 298 K (dots and lines) and (b) the isosteric enthalpies of SF_6 adsorption for the TBAPy-MOFs.
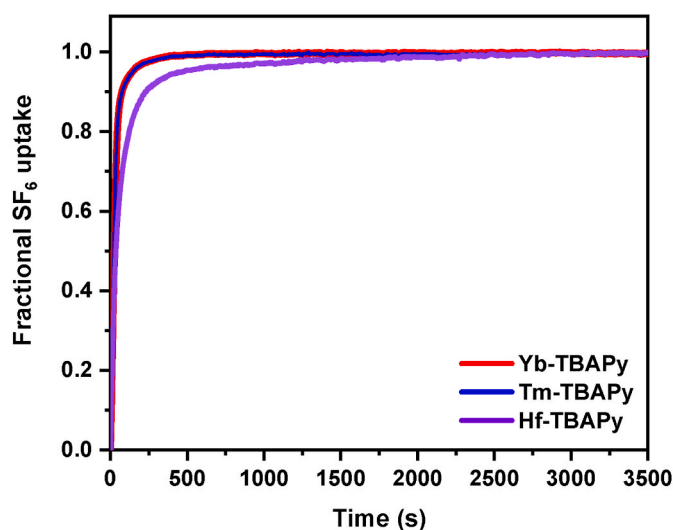

Fig. 7. Gravimetric SF_6 adsorption profiles of the MOFs recorded at 303 K and on approx. 15 mg of sample.

Table 3
Calculated SF_6 diffusivities obtained from the intracrystalline diffusion model.

Sample	Intracrystalline diffusion model, short-time D_i (s^{-1})	Intracrystalline diffusion model, long-time D_i (s^{-1})
Yb-TBAPy	6.22×10^{-4}	5.54×10^{-4}
Tm-TBAPy	6.33×10^{-4}	5.08×10^{-4}
Hf-TBAPy	5.66×10^{-4}	3.34×10^{-4}

the same magnitude as the SF_6 diffusivities in other porous sorbents such as SU-101 and CAU-17 [46]. It is important to note that the calculated values should be taken as a rough estimate of the SF_6 diffusivity in the TBAPy-MOFs due to the discrepancy between the experimentally observed data and the theoretical model.

4. Conclusions

Four metal-organic frameworks based on Yb-, Tm-, Ce-, and Hf-TBAPy were synthesized in this study. The four MOFs have structures that resemble either JXNU-5, ROD-7, or NU-1000 previously reported. The SF_6 adsorption properties of these Yb- Tm- and Hf-TBAPy-MOFs

were examined. These MOFs were found to selectively adsorb SF_6-over-N_2 with IAST high selectivity of up to ~50 (303 K, 100 kPa, in 10:90 SF_6:N_2) and high SF_6 uptake of over 2.61 mmol g^{-1} (273 K, 100 kPa). Yb- and Tm-TBAPy had suitable pore sizes of ~0.65 nm that can result in the enhanced interaction with SF_6 and the selective adsorption of SF_6. Isosteric enthalpies of SF_6 adsorption was also calculated to be within the physisorption range and all TBAPy-MOFs showed good cyclic stability. The SF_6 adsorption was also found to occur relatively rapidly on all MOFs and 80% of the total uptake capacity was reached within 3 min. Furthermore, the SF_6 diffusivity was found to range from ~3 – 6 × 10^{-4} s^{-1}. We demonstrate that TBAPy-MOFs possess a number of desirable properties that make them candidate adsorbents for further development, including good chemical and thermal stability and high porosities. It could be interesting to further develop TBAPy-MOFs for application using post-synthesis structural processing, such as pelletization or formulation for 3D printing.

CRediT authorship contribution statement

Michelle Åhlén: Writing – review & editing, Writing – original draft, Methodology, Investigation, Formal analysis, Data curation, Conceptualization. **Francoise M. Amombo Noa:** Writing – review & editing, Formal analysis, Data curation. **Lars Öhrström:** Writing – review & editing, Formal analysis, Data curation. **Daniel Hedbom:** Writing – review & editing, Methodology, Data curation. **Maria Strømme:** Writing – review & editing, Supervision, Funding acquisition. **Ocean Cheung:** Writing – review & editing, Writing – original draft, Supervision, Resources, Project administration, Methodology, Investigation, Funding acquisition, Formal analysis, Data curation, Conceptualization.

Declaration of competing interest

The authors declare that they have no known competing financial interests or personal relationships that could have appeared to influence the work reported in this paper.

Data availability

Data will be made available on request.

Acknowledgement

Dhruva Deole of Uppsala University is acknowledged for his assistance in materials synthesis. Michal Strach and Chalmers Materials Analysis Laboratory is acknowledged for help in material analysis.

Appendix A. Supplementary data

Supplementary data to this article can be found online at https://doi.org/10.1016/j.micromeso.2022.112161.

References

[1] W.-T. Tsai, *The decomposition products of sulfur hexafluoride (SF6): Reviews of environmental and health risk analysis*, J. Fluor. Chem. 128 (2007) 1345–1352, https://doi.org/10.1016/j.jfluchem.2007.06.008.

[2] S. Prodinger, R.S. Vemuri, T. Varga, P.B. McGrail, R.K. Motkuri, M.A. Derewinski, *Impact of chabazite SSZ-13 textural properties and chemical composition on CO2 adsorption applications*, New J. Chem. 40 (2016) 4375–4385, https://doi.org/10.1039/C5NJ03205A.

[3] O. Cheung, Z. Bacsik, Q. Liu, A. Mace, N. Hedin, *Adsorption kinetics for CO2 on highly selective zeolites NaKA and nano-NaKA*, Appl. Energy 112 (2013) 1326–1336, https://doi.org/10.1016/j.apenergy.2013.01.017.

[4] H. Zhang, Z. Wang, X. Luo, J. Lu, S. Peng, Y. Wang, L. Han, *Constructing hierarchical porous carbons with interconnected micro-mesopores for enhanced CO2 adsorption*, Front. Chem. 7 (2019) 919, https://doi.org/10.3389/fchem.2019.00919.

[5] S. Jung, Y.-K. Park, E.E. Kwon, *Strategic use of biochar for CO2 capture and sequestration*, J. CO2 Util. 32 (2019) 128–139, https://doi.org/10.1016/j.jcou.2019.04.012.

[6] M. Ding, R.W. Flaig, H.-L. Jiang, O.M. Yaghi, Carbon capture and conversion using metal-organic frameworks and MOF-based materials, Chem. Soc. Rev. 48 (2019) 2783–2828, https://doi.org/10.1039/C8CS00829A.

[7] R. Aniruddha, I. Sreedhar, B.M. Reddy, MOFs in carbon capture-past, present and future, J. CO2 Util. 42 (2020), 101297, https://doi.org/10.1016/j.jcou.2020.101297.

[8] R.L. Siegelman, E.J. Kim, J.R. Long, Porous materials for carbon dioxide separations, Nat. Mater. 20 (2021) 1060–1072, https://doi.org/10.1038/s41563-021-01054-8.

[9] Q. Wang, D. Astruc, State of the art and prospects in metal-organic framework (MOF)-Based and MOF-derived nanocatalysis, Chem. Rev. 120 (2020) 1438–1511, https://doi.org/10.1021/acs.chemrev.9b00223.

[10] J.-D. Xiao, H.-L. Jiang, Metal-organic frameworks for photocatalysis and photothermal catalysis, Acc. Chem. Res. 52 (2019) 356–366, https://doi.org/10.1021/acs.accounts.8b00521.

[11] Y. Cui, B. Chen, G. Qian, Lanthanide metal-organic frameworks for luminescent sensing and light-emitting applications, Coord. Chem. Rev. 273–274 (2014) 76–86, https://doi.org/10.1016/j.ccr.2013.10.023.

[12] W.P. Lustig, S. Mukherjee, N.D. Rudd, A.V. Desai, J. Li, S.K. Ghosh, Metal-organic frameworks: functional luminescent and photonic materials for sensing applications, Chem. Soc. Rev. 46 (2017) 3242–3285, https://doi.org/10.1039/C6CS00930A.

[13] Y. Sun, L. Zheng, Y. Yang, X. Qian, T. Fu, X. Li, Z. Yang, H. Yan, C. Cui, W. Tan, Metal-organic framework nanocarriers for drug delivery in biomedical applications, Nano-Micro Lett. 12 (2020) 103, https://doi.org/10.1007/s40820-020-00423-3.

[14] T. Qiu, Z. Liang, W. Guo, H. Tabassum, S. Gao, R. Zou, Metal–organic framework-based materials for energy conversion and storage, ACS Energy Lett. 5 (2020) 520–532, https://doi.org/10.1021/acsenergylett.9b02625.

[15] F.P. Kinik, A. Ortega-Guerrero, D. Ongari, C.P. Ireland, B. Smit, Pyrene-based metal organic frameworks: from synthesis to applications, Chem. Soc. Rev. 50 (2021) 3143–3177, https://doi.org/10.1039/d0cs00424c.

[16] S.S. Park, C.H. Hendon, A.J. Fielding, A. Walsh, M. O'Keeffe, M. Dincă, The organic secondary building unit: strong intermolecular pi interactions define topology in MIT-25, a mesoporous MOF with proton-replete channels, J. Am. Chem. Soc. 139 (2017) 3619–3622, https://doi.org/10.1021/jacs.6b13176.

[17] A. Gładysiak, T.N. Nguyen, R. Bounds, A. Zacharia, G. Itskos, J.A. Reimer, K.C. Stylianou, Temperature-dependent interchromophoric interaction in a fluorescent pyrene-based metal-organic framework, Chem. Sci. 10 (2019) 6140–6148, https://doi.org/10.1039/c9sc01422e.

[18] Z. Hu, C. Qiao, Z. Xia, F. Li, J. Han, Q. Wei, Q. Yang, G. Xie, S. Chen, S. Gao, A luminescent Mg-metal-organic framework for sustained release of 5-fluorouracil: appropriate host-guest interaction and satisfied acid-base resistance, ACS Appl. Mater. Interfaces 12 (2020) 14914–14923, https://doi.org/10.1021/acsami.0c01198.

[19] K.C. Stylianou, J. Rabone, S.Y. Chong, R. Heck, J. Armstrong, P.V. Wiper, K.E. Jelfs, S. Zlatogorsky, J. Bacsa, A.G. McLennan, C.P. Ireland, Y.Z. Khimyak, K.M. Thomas, D. Bradshaw, M.J. Rosseinsky, Dimensionality transformation through

[20] O. Karagiaridi, W. Bury, D. Fairen-Jimenez, C.E. Wilmer, A.A. Sarjeant, J.T. Hupp, O.K. Farha, Enhanced gas sorption properties and unique behavior toward liquid water in a pillared-paddlewheel metal-organic framework transmetalated with Ni (II), Inorg. Chem. 53 (2014) 10432–10436, https://doi.org/10.1021/ic501467w.

[21] A.V. Vinogradov, H. Zaake-Hertling, A.S. Drozdov, P. Lönnecke, G.A. Seisenbaeva, V.G. Kessler, V.V. Vinogradova, E. Hey-Hawkins, Anomalous adsorption of biomolecules on a Zn-based metal-organic framework obtained via a facile room-temperature route, Chem. Commun. 51 (2015) 17764–17767, https://doi.org/10.1039/c5cc07808c.

[22] J.-H. Qin, Y.-D. Huang, Y. Zhao, X.-G. Yang, F.-F. Li, C. Wang, L.-F. Ma, Highly dense packing of chromophoric linkers achievable in a pyrene-based metal-organic framework for photoelectric response, Inorg. Chem. 58 (2019) 15013–15016, https://doi.org/10.1021/acs.inorgchem.9b02203.

[23] K.C. Stylianou, J. Bacsa, D. Bradshaw, M.J. Rosseinsky, A 3D porous metal organic framework based on infinite 1D nickel(II) chains with rutile topology displaying open metal sites, Z. Anorg. Allg. Chem. 640 (2014) 2123–2131, https://doi.org/10.1002/zaac.201400136.

[24] K.C. Stylianou, R. Heck, S.Y. Chong, J. Bacsa, J.T.A. Jones, Y.Z. Khimyak, D. Bradshaw, M.J. Rosseinsky, A guest-responsive fluorescent 3D microporous metal−organic framework derived from a long-lifetime pyrene core, J. Am. Chem. Soc. 132 (2010) 4119–4130, https://doi.org/10.1021/ja906041f.

[25] R. Liu, Q.-Y. Liu, R. Krishna, W. Wang, C.-T. He, Y.-L. Wang, *Water-stable europium 1,3,6,8-tetrakis(4-carboxylphenyl)pyrene framework for efficient C2H2/CO2 separation*, Inorg. Chem. 58 (2019) 5089–5095, https://doi.org/10.1021/acs.inorgchem.9b00169.

[26] J.E. Mondloch, W. Bury, D. Fairen-Jimenez, S. Kwon, E.J. DeMarco, M.H. Weston, A.A. Sarjeant, S.T. Nguyen, P.C. Stair, R.Q. Snurr, O.K. Farha, J.T. Hupp, Vapor-phase metalation by atomic layer deposition in a metal-organic framework, J. Am. Chem. Soc. 135 (2013) 10294–10297, https://doi.org/10.1021/ja4050828.

[27] H. Beyzavi, R.C. Klet, S. Tussupbayev, J. Borycz, N.A. Vermeulen, C.J. Cramer, J.F. Stoddart, J.T. Hupp, O.m.K. Farha, *A hafnium-based metal-organic framework as an efficient and multifunctional catalyst for facile CO2 fixation and regioselective and enantioretentive epoxide activation*, J. Am. Chem. Soc. 136 (2014) 15861–15864, https://doi.org/10.1021/ja508626n.

[28] P. Li, N.A. Vermeulen, X. Gong, C.D. Malliakas, J.F. Stoddart, J.T. Hupp, O.K. Farha, Design and synthesis of a water-stable anionic uranium-based metal-organic framework (MOF) with ultra large pores, Angew. Chem. Int. Ed. Engl. 55 (2016) 10358–10362, https://doi.org/10.1002/anie.201605547.

[29] J. Ai, F.-Y. Chen, C.-Y. Gao, H.-R. Tian, Q.-J. Pan, Z.-M. Sun, *Porous anionic uranyl-organic networks for highly efficient Cs+ adsorption and investigation of the mechanism*, Inorg. Chem. 57 (2018) 4419–4426, https://doi.org/10.1021/acs.inorgchem.8b00099.

[30] R.-J. Li, M. Li, X.-P. Zhou, S.W. Ng, M. O'Keeffe, D. Li, ROD-8, a rod MOF with a pyrene-cored tetracarboxylate linker: framework disorder, derived nets and selective gas adsorption, CrystEngComm 16 (2014) 6291–6295, https://doi.org/10.1039/c4ce00279b.

[31] R.-J. Li, M. Li, X.-P. Zhou, D. Li, M. O'Keeffe, *A highly stable MOF with a rod SBU and a tetracarboxylate linker: unusual topology and CO2 adsorption behaviour under ambient conditions*, Chem. Commun. 50 (2014) 4047–4049, https://doi.org/10.1039/c3cc49684h.

[32] T. Islamoglu, K.-i. Otake, P. Li, C.T. Buru, A.W. Peters, I. Akpinar, S.J. Garibay, O.K. Farha, Revisiting the structural homogeneity of NU-1000, a Zr-based metal–organic framework, CrystEngComm 20 (2018) 5913–5918, https://doi.org/10.1039/c8ce00455b.

[33] A.C. Sudik, A.R. Millward, N.W. Ockwig, A.P. Côté, J. Kim, O.M. Yaghi, *Design, synthesis, structure, and gas (N2, Ar, CO2, CH4, and H2) sorption properties of porous metal-organic tetrahedral and heterocuboidal polyhedra*, J. Am. Chem. Soc. 127 (2005) 7110–7118, https://doi.org/10.1021/ja042802q.

[34] R.M. de Vos, H. Verweij, Improved performance of silica membranes for gas separation, J. Membr. Sci. 143 (1998) 37–51, https://doi.org/10.1016/S0376-7388(97)00334-7.

[35] P.G. Boyd, A. Chidambaram, E. García-Díez, C.P. Ireland, T.D. Daff, R. Bounds, A. Gładysiak, P. Schouwink, S.M. Moosavi, M.M. Maroto-Valer, J.A. Reimer, J.A.R. Navarro, T.K. Woo, S. Garcia, K.C. Stylianou, B. Smit, *Data-driven design of metal-organic frameworks for wet flue gas CO2 capture*, Nature 576 (2019) 253–256, https://doi.org/10.1038/s41586-019-1798-7.

[36] D.W. Breck, Zeolite Molecular Sieves - Structure, Chemistry and Use, John Wiley & Sons, New York, 1974.

[37] J.W.M. Osterrieth, J. Rampersad, David G. Madden, N. Rampal, L. Skoric, B. Connolly, M.D. Allendorf, V. Stavila, J.L. Snider, R. Ameloot, J. Marreiros, C. Ania, D. Azevedo, E. Vilarrasa-Garcia, B.F. Santos, X.-H. Bu, Z. Chang, H. Bunzen, N.R. Champness, S.L. Griffin, B. Chen, R.-B. Lin, B. Coasne, S. Cohen, J.C. Moreton, Y.J. Colón, L. Chen, R. Clowes, F.-X. Coudert, Y. Cui, B. Hou, D.M. D'Alessandro, P.W. Doheny, M. Dincă, C. Sun, C. Doonan, M.T. Huxley, J.D. Evans, P. Falcaro, R. Ricco, O. Farha, K.B. Idrees, T. Islamoglu, P. Feng, H. Yang, R.S. Forgan, D. Bara, S. Furukawa, E. Sanchez, J. Gascon, S. Telalović, S.K. Ghosh, S. Mukherjee, M.R. Hill, M.M. Sadiq, P. Horcajada, P. Salcedo-Abraira, K. Kaneko, R. Kukobat, J. Kenvin, S. Keskin, S. Kitagawa, K.-i. Otake, R.P. Lively, S.J.A. DeWitt, P. Llewellyn, B.V. Lotsch, S.T. Emmerling, A.M. Pütz, C. Martí-Gastaldo, N.M. Padial, J. García-Martínez, N. Linares, D. Maspoch, J.A. Suárez del Pino, P. Moghadam, R. Oktavian, R.E. Morris, P.S. Wheatley, J. Navarro, C. Petit, D. Danaci, M.J. Rosseinsky, A.P. Katsoulidis, M. Schröder, X. Han, S. Yang, C. Serre, G. Mouchaham, D.S. Sholl, R. Thyagarajan, D. Siderius, R.Q. Snurr, R.

B. Goncalves, S. Telfer, S.J. Lee, V.P. Ting, J.L. Rowlandson, T. Uemura, T. Iiyuka, M.A. van der Veen, D. Rega, V. Van Speybroeck, S.M.J. Rogge, A. Lamaire, K. S. Walton, L.W. Bingel, S. Wuttke, J. Andreo, O. Yaghi, B. Zhang, C.T. Yavuz, T. S. Nguyen, F. Zamora, C. Montoro, H. Zhou, A. Kirchon, D. Fairen-Jimenez, How reproducible are surface areas calculated from the BET equation? Adv. Mater. (2022), e2201502 https://doi.org/10.1002/adma.202201502.

[38] A.L. Myers, J.M. Prausnitz, Thermodynamics of mixed-gas adsorption, AIChE J. 11 (1965) 121–127, https://doi.org/10.1002/aic.690110125.

[39] H. Pan, J.A. Ritter, P.B. Balbuena, Examination of the approximations used in determining the isosteric heat of adsorption from the Clausius-Clapeyron equation, Langmuir 14 (1998) 6323–6327, https://doi.org/10.1021/la9803373.

[40] D.M. Ruthven, Principles of Adsorption and Adsorption Processes, John Wiley Sons Inc., New Jersey, 1984.

[41] M. Thommes, K. Kaneko, A.V. Neimark, J.P. Olivier, F. Rodriguez-Reinoso, J. Rouquerol, K.S.W. Sing, Physisorption of gases, with special reference to the evaluation of surface area and pore size distribution (IUPAC Technical Report), Pure Appl. Chem. 87 (2015) 1051–1069, https://doi.org/10.1515/pac-2014-1117.

[42] T.N. Tu, H.T.T. Nguyen, H.T.D. Nguyen, M.V. Nguyen, T.D. Nguyen, N.T. Tran, K. T. Lim, A new iron-based metal–organic framework with enhancing catalysis activity for benzene hydroxylation, RSC Adv. 9 (2019) 16784–16789, https://doi.org/10.1039/c9ra03287h.

[43] M. Åhlén, A. Jaworski, M. Strømme, O. Cheung, *Selective adsorption of CO$_2$ and SF$_6$ on mixed-linker ZIF-7–8s: The effect of linker substitution on uptake capacity and kinetics*, Chem. Eng. J. 422 (2021), 130117, https://doi.org/10.1016/j.cej.2021.130117.

[44] I. Senkovska, E. Barea, J.A.R. Navarro, S. Kaskel, Adsorptive capturing and storing greenhouse gases such as sulfur hexafluoride and carbon tetrafluoride using metal–organic frameworks, Microporous Mesoporous Mater. 156 (2012) 115–120, https://doi.org/10.1016/j.micromeso.2012.02.021.

[45] M.-B. Kim, T.-U. Yoon, D.-Y. Hong, S.-Y. Kim, S.-J. Lee, S.-I. Kim, S.-K. Lee, J.-S. Chang, Y.-S. Bae, *High SF$_6$/N$_2$ selectivity in a hydrothermally stable zirconium-based metal–organic framework*, Chem. Eng. J. 276 (2015) 315–321, https://doi.org/10.1016/j.cej.2015.04.087.

[46] M. Åhlén, E. Kapaca, D. Hedbom, T. Willhammar, M. Strømme, O. Cheung, *Gas sorption properties and kinetics of porous bismuth-based metal-organic frameworks and the selective CO$_2$ and SF$_6$ sorption on a new bismuth trimesate-based structure UU-200*, Microporous Mesoporous Mater. 329 (2022), https://doi.org/10.1016/j.micromeso.2021.111548.

[47] M.-B. Kim, S.-J. Lee, C.Y. Lee, Y.-S. Bae, *High SF$_6$ selectivities and capacities in isostructural metal-organic frameworks with proper pore sizes and highly dense unsaturated metal sites*, Microporous Mesoporous Mater. 190 (2014) 356–361, https://doi.org/10.1016/j.micromeso.2014.02.028.

[48] E. Svensson Grape, H. Xu, O. Cheung, M. Calmels, J. Zhao, C. Dejoie, D. M. Proserpio, X. Zou, A.K. Inge, Breathing metal–organic framework based on flexible inorganic building units, Cryst. Growth Des. 20 (2019) 320–329, https://doi.org/10.1021/acs.cgd.9b01266.

[49] R. Sun, C.-W. Tai, M. Strømme, O. Cheung, *Hierarchical porous carbon synthesized from novel porous amorphous calcium or magnesium citrate with enhanced SF$_6$ uptake and SF$_6$/N$_2$ selectivity*, ACS Appl. Nano Mater. 2 (2019) 778–789, https://doi.org/10.1021/acsanm.8b02005.

[50] B. Wang, H. Huang, X.-L. Lv, Y. Xie, M. Li, J.-R. Li, *Tuning CO$_2$ selective adsorption over N$_2$ and CH$_4$ in UiO-67 analogues through ligand functionalization*, Inorg. Chem. 53 (2014) 9254–9259, https://doi.org/10.1021/ic5013473.

[51] P. Nugent, Y. Belmabkhout, S.D. Burd, A.J. Cairns, R. Luebke, K. Forrest, T. Pham, S. Ma, B. Space, L. Wojtas, M. Eddaoudi, M.J. Zaworotko, *Porous materials with optimal adsorption thermodynamics and kinetics for CO$_2$ separation*, Nature 495 (2013) 80–84, https://doi.org/10.1038/nature11893.

[52] H.-S. Choi, M.P. Suh, *Highly selective CO$_2$ capture in flexible 3D coordination polymer networks*, Angew. Chem. Int. Ed. Engl. 48 (2009) 6865–6869, https://doi.org/10.1002/anie.200902836.

[53] S.-N. Kim, J. Kim, H.-Y. Kim, H.-Y. Cho, W.-S. Ahn, *Adsorption/catalytic properties of MIL-125 and NH$_2$-MIL-125*, Catal. Today 204 (2013) 85–93, https://doi.org/10.1016/j.cattod.2012.08.014.

[54] V.K. Singh, E. Anil Kumar, *Measurement and analysis of adsorption isotherms of CO$_2$ on activated carbon*, Appl. Therm. Eng. 97 (2016) 77–86, https://doi.org/10.1016/j.applthermaleng.2015.10.052.